A 19 GHz Lithium Niobate Acoustic Filter with FBW of 2.4%

Liuqing Gao, Yansong Yang, and Songbin Gong University of Illinois at Urbana-Champaign, IL, USA lgao13@illinois.edu, yyang165@illinois.edu, songbin@illinois.edu

Abstract—This paper presents the first demonstration of a wideband hybrid monolithic acoustic filter in the K-band which exceeds the limitation of electromechanical coupling on the fractional bandwidth (FBW) of acoustic filters. The hybrid filter utilizes the co-design of EM and acoustic to attain wide bandwidth while keeping the advantages of small sizes and high Q in the acoustic domain. The fabricated filter built with resonators having an electromechanical coupling of 0.7% based on the seventh-order antisymmetric Lamb wave mode (A7) has a 3 dB FBW of 2.4% at 19 GHz, and a compact footprint of 1.4 mm^2 .

Keywords— Microelectromechanical systems, millimeter-wave devices, piezoelectric devices, K-band

I. Introduction

As the sub-6G spectrum becomes over-crowded with applications, the research community starts to explore beyond 6 GHz for new spectral venues to advance wireless capabilities. Several bands ranging from 12 GHz to 27 GHz have been proposed [1], sharing the same challenge in scaling conventional frontend components well beyond their current operating frequencies. One indispensable front-end component that is particularly difficult to scale in frequency is the acoustic filters that have been commercially successful for 4G [2], [3]. Frequency scaling without compromising performance remains difficult due to various technical bottlenecks in material integration, device fabrication, and filter design for acoustic filters.

The scaling approaches so far can be classified into two categories. The first type resorts to the reduction in feature size for increasing the center frequency (e.g., electrode width or lateral mode or film thickness for thickness mode devices) [4], [5]. However, excessive thickness or size reduction often leads to poor film quality for the acoustic material or higher electrode resistance, consequently resulting in higher insertion loss (IL), degraded power handling, and more severe non-linearity. The other type of approaches adopts higher order of acoustic resonant modes (i.e., overmoding) while maintaining the sizes of the resonant cavity and other device features in the process of scaling [6], [7]. Unfortunately, these approaches face the loss of electromechanical coupling $(k_t^2 \sim l/f^2 \text{ in scaling})$ and hence trade FBW off for a higher center frequency. In particular, scaling 4G acoustic filters based on surface-acoustic-wave (SAW) and film-bulk-acoustic-resonators (FBAR) towards 20 GHz and beyond by overmoding might be more penalizing than rewarding. Their electromechanical coupling of respectively 10% and 6.5% would be reduced too much to recover from for anything other than extreme narrowband applications.

Recently, asymmetric Lamb wave micro-acoustic resonators based on LiNbO₃ have been shown with significantly larger k_t^2 of 30%, thus allowing better trades between k_t^2 and fre-

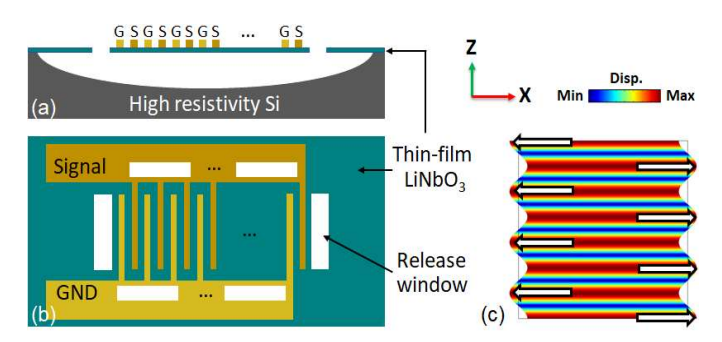


Fig. 1. (a) Cross-section and (b) top views of a thin-film Z-cut LiNbO₃ resonator with multiple interdigital electrodes. (c) Displacement mode shape of the seventh-order antisymmetric Lamb wave mode (A7).

quency scaling. Researchers have indeed demonstrated higherorder asymmetric resonators up to 30 GHz with Qs of 400 and filter up to 10 GHz with IL of 3 dB. However, the fractional bandwidth (FBW) of the 10 GHz acoustic filter is only 0.7% due to the aforementioned design trade [8]. To overcome the k_t^2 loss in scaling and recover the FBW loss, this work co-designs acoustic and EM structures in tandem to enhance the FBW while still harnessing the small-size and high O in the acoustics domain. The principle behind our approach is to use the acoustic resonance in conjunction with an inductive element as the building blocks for constructing a ladder filter [9], [10]. The inductor can equivalently recover some of the k_t^2 loss, enhance the FBW, and introduce an additional anti-resonance without harshly compromising IL and roll-off of the filter. Its effect has been similarly explored using the framework of coupled modes for lower-frequency hybrid filters that combine acoustic resonator with inadequate k_t^2 and lumped elements [11]. However, the added value at lower frequencies for this approach comes at the expense of larger sizes as substantial inductances are typically needed. High-frequency adaptation of a hybrid filter has not been demonstrated (largely due to the absence of 20 GHz acoustic resonators) despite that it needs much smaller inductance for the same purpose and does not add significant size.

In this work, we develop a hybrid filter design that combines chip-scale reactive elements with A7 mode LiNbO₃ resonator at 19 GHz. As a result of our co-design effort, this work widens the FBW of acoustic filters and demonstrates an acoustic filter with 2.4% FBW while only using resonators with 0.7% k_t^2 and occupying a small footprint of 1.4 mm².

II. CO-DESIGN OF ACOUSTICS AND EM STRUCTURES

A. Inductor Induced BW Enhancement for Acoustic Resonator

The mock-up of a Z-cut thin-film LiNbO₃ resonator is shown in Fig. 1(a) and (b). The resonance of the antisymmetric

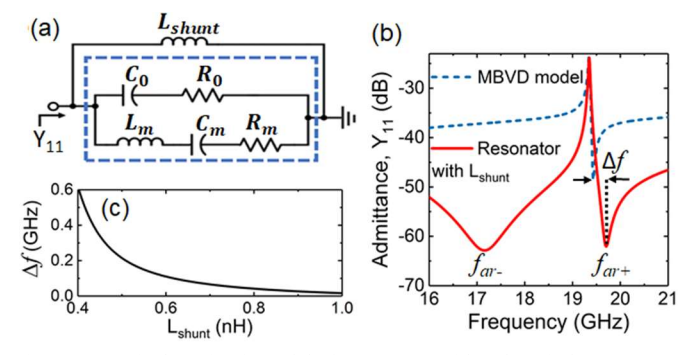


Fig. 2. (a) Equivalent circuit model of a resonator with a shunt inductor (L_{shunt}). (b) Admittances of a resonator with and without a L_{shunt} . (c) Spectral offset of the anti-resonance frequency (Δf) versus L_{shunt} .

Lamb wave mode is governed by the mode order (m), film thickness (t), separation between adjacent interdigital electrodes (l), and acoustic phase velocities in the vertical (v_t) and longitudinal (v_L) directions which can be expressed by:

$$f_{r,m} = \sqrt{(m\frac{v_t}{2t})^2 + (\frac{v_L}{2l})^2}$$
 (1)

In this work, t of 650 nm, t of 3 μ m are selected considering the power handling and fabrication capability. In order for the resonator to operate in the K-band, A7 mode is selected. The ratio of k_t^2 of the higher ordered asymmetric mode to that of A1 is inversely proportional to the square of the mode number. A simple ladder acoustics filter would have an FBW that narrows at a rate inversely proportional to the square of the increasing center frequency. As a result, a ladder filter constructed with A7 will have an FBW of 0.35%, leading to few applications due to the extremely narrow bandwidth.

Connecting a shunt inductor to an acoustic resonator is a well-known technique to enlarge the spectral separation between the series and parallel resonances of the circuit, equivalent to the effect of increasing k_t^2 of the resonator but without the benefit of a larger impedance ratio (Z_{as}/Z_s). Such an effect can be modelled by representing the acoustic resonator with Modified Butterworth-Van Dyke (MBVD) model in a circuit comprising an acoustic resonator and shunt inductor as seen in Fig. 2(a). L_{shunt} denotes the shunt inductor, C_0 denotes the static capacitance, R_0 represents the loss in LiNbO₃ film, and R_m , C_m , L_m electrically represent the motional branch and mechanical resonance. The admittances of a resonator with and without a shunt resonator are plotted in Fig. 2(b). The anti-resonance (f_{ar+}) of the circuit is shifted by L_{shunt} to a higher frequency than the anti-resonance of the acoustic resonator (f_{ar}) , producing a larger BW that can be similarly achieved with a higher k_t^2 acoustic resonator. The inclusion of L_{shunt} also induces an additional antiresonance at a lower frequency (f_{ar}) that results from a second solution where L_{shunt} and L_m collaboratively tune out C_m and C_0 .

The resonance (f_r) and anti-resonances $(f_{ar\pm})$ of the circuit can be theoretically calculated. Due to the low loss tangent of LiNbO₃, the influence of substrate loss on f_r and $f_{ar\pm}$ is negligible, and the input admittance (Y_{II}) looking into the port shown in Fig. 2(b) can be expressed by:

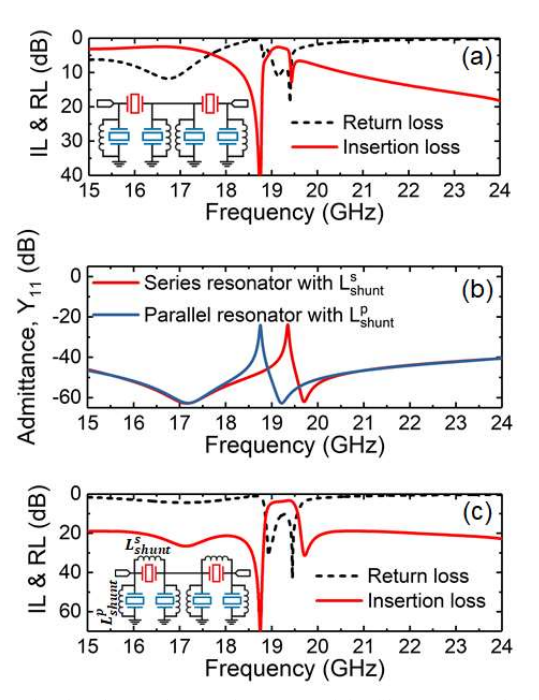


Fig. 3. (a) Simulated IL and return loss (RL) of the filter composed of parallel resonators with L^p_{shunt} and stand-alone series resonators, as seen in the inset. (b) Simulated admittances of parallel and series resonators both with shunt inductors. (c) Simulated IL and RL of the filter shown in the inset.

$$Y_{11} = \frac{\frac{L_m}{C_0} - \frac{1}{\omega^2 C_0 C_m} - \omega^2 L_m L_{shunt} + L_{shunt} \cdot \left[\frac{1}{C_m} + \frac{1}{C_0} \right]}{j\omega L_{shunt} \cdot \left[\frac{L_m}{C_0} - \frac{1}{\omega^2 C_0 C_m} \right]}$$
(2)

where f_r is the frequency at which the denominator equates zero, and $f_{ar\pm}$ are the frequencies at which the numerator equates zero. The closed-form expressions of f_r and $f_{ar\pm}$ are:

$$f_r = \frac{1}{2\pi\sqrt{L_mC_m}}\tag{3}$$

$$f_{ar\pm} = \frac{1}{2\pi} \sqrt{\frac{b \pm \sqrt{b^2 - 4L_m L_{shunt} C_0 C_m}}{2L_m L_{shunt} C_0 C_m}}$$
(4)

$$b = L_m C_m + L_{shunt} (C_m + C_0)$$
 (5)

 Δf is defined as the spectral separation between the f_{ar+} and f_{ar} . For a resonator at 19.15 GHz with k_t^2 of 0.7%, and C_0 of 114 fF, its Δf versus L_{shunt} is plotted in Fig. 2(c), which is used to determine the L_{shunt} value during the filter design for a target Δf .

B. Co-Design Procedure

To fully harness the benefit of a virtually increased kt^2 of a resonator by a shunt inductor for constructing a filter with wider FBW, the offset between the resonances of series and parallel resonators is increased by Δf . This creates a challenge in the implementation of the design, as adjusting the lateral dimensions of the interdigital electrodes only gives a limited amount of offset. Thus, we opt for trimming the film thickness, which as seen in Eq. 1 dominantly affects the resonance. This is the first demonstration of this monolithic technique to create an increased resonance offset.

Table 1. Key Circuit Simulation Parameters of the Resonators and Filter.

	Frequency (GHz)	Resonator Q	Co (fF)	kt ²	$R_m(\Omega)$	Cm (fF)	L_m (nH)	Lshunt (nH)	Inductor Q
Parallel Resonator	18.75	500	125	0.7%	23.93	0.709	101.5	0.77	30
Series Resonator	19.15	500	114	0.7%	25.70	0.647	106.8	0.66	30

Table 2. Design Parameters of the Filter.

Design Parameter	Dimension			
Electrode length	55 μm			
Electrode width	3 μm			
Electrode separation	3 μm			
Number of electrodes	40			
Side length of L_{shunt}^p	337 μm			
Width of L_{shunt}^p	20 μm			
Side length of L_{shunt}^{s} (l_{s})	282 μm			
Width of L_{shunt}^{s} (w_{s})	20 μm			

Consider a filter constructed with only shunt inductors (L_{shu}^p) connected to the parallel resonators, and as can be seen in Fig. 3(a), the stopband filter performance is deteriorated. To improve the stopband filter performance, shunt inductors (L_{shunt}^s) are connected to series resonators to decrease the admittance through the series branch in the stopband, as shown in Fig. 3(b). As a result, most of the input power gets reflected in stopband due to impedance mismatching. From the plot of filter IL and RL in Fig. 3(c), the stopband performance is greatly improved. The key design parameters in the circuit models in this section are listed in Table 1.

C. Finite Element Simulation of MEMS Resonators and Filters

At high frequencies, the self-inductance from the lead lines and electrodes of a MEMS resonator is no longer negligible. Along with the static capacitance, it introduces a self-resonance that masks acoustic resonant response. Consequently, the power transmitted through the mechanical coupling between the interdigital electrodes can be significantly reduced.

The self-resonance frequency of a MEMS resonator is dependent on the number of electrodes, electrode length, width, and separation. To predict and increase the self-resonance, the high-frequency EM response from the electrode layout of the acoustic resonator is studied with Momentum simulation. Since our target operating frequency is at 19 GHz, an electrode layout with an electrical self-resonance at 40 GHz is targeted for mitigating its influence on our filter performance.

In addition to the self-inductance, the parasitic effects and couplings in the layout can also be significant, which must be considered in the filter design. However, commercial modeling solutions do not support finite element analysis (FEA) that couples EM and acoustic simulations at drastically different scales. Therefore, the co-design of the filter layout is done by first performing EM simulation in Momentum and then adding motional branches derived from acoustic FEA to fully capture effects in layouts and acoustics in Advanced Design System (ADS). The C_0 and R_0 from EM simulations are consistent with those from COMSOL-based FEA, which validates this method. The design parameters of the filter are listed in Table 2. The

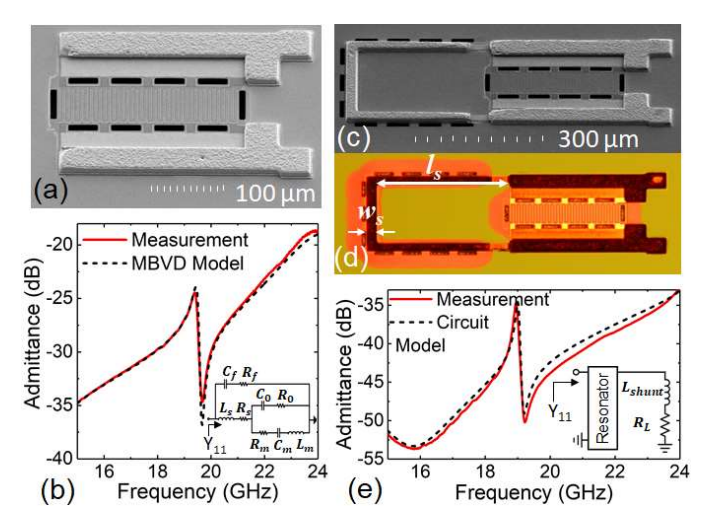


Fig. 4. (a) SEM image and (b) measurement and circuit model of the fabricated resonator. (c) SEM and (d) optical microscope images, and (e) measured and circuit modeled responses of the fabricated resonator with a shunt inductor.

physical dimensions (l_s and w_s) of L_{shunt}^s are marked in Fig. 5(b).

III. MEASUREMENT RESULTS AND DISCUSSION

The devices were fabricated with a standard thin-film LiNbO₃ MEMS resonator fabrication process on a 650 nm thick thin film Z-cut LiNbO₃ on a high resistivity Si wafer. The desired offset between the resonances of series and parallel resonators is achieved by regionally thinning the LiNbO3 film where the series resonators are situated [12]. Such a technique permits shifting the resonance to a higher frequency. The film is thinned down from 650 nm to 620 nm, creating a resonance offset of 400 MHz. To reduce electric loss, the inductors, lead lines and probing pads (i.e., regions other the acoustic resonator cavity) are thickened with an additional step of copper electroplating, as seen in Fig. 4(a). In addition, the inductors, as shown in Fig. 4(d) are also suspended to reduce the substrate loss caused by the magnetically induced Eddy current in the Si substrate. For performance diagnosis purposes, comprising structures, such as a stand-alone resonator with and without a shunt inductor, were also fabricated along with the filter. The measurement results of these comprising structures and the MEMS filter are reported and analyzed in this section.

A. Comprising Structures

The SEM image and measured response of the fabricated stand-alone resonator are shown in Fig. 4(a) and (b). The measured response is fitted by the MBVD model with additional branches taking the self-inductance (L_s) and parasitic capacitance (C_f) into account. The parameters extracted from the circuit fitting that quantifies the resonator A7 mode response are: resonance at 19.6 GHz, resonator Q of 146, k_t^2 of 0.7%, C_0 of 125 fF, L_s of 0.15 nH, and C_f of 34 fF.

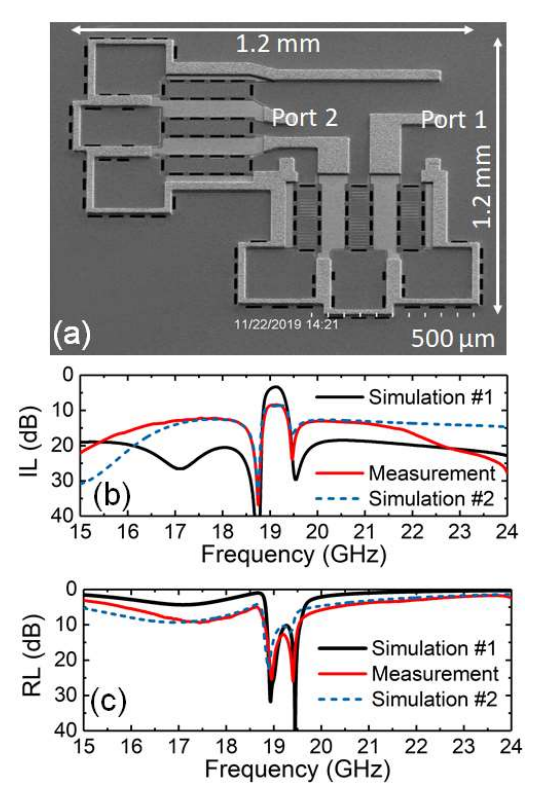


Fig. 5. (a) SEM image of the fabricated filter. (b) IL and (c) RL of the measured and simulated performance of the fabricated MEMS filter.

The measured L_s is three times larger than the simulated value. As a result, the self-resonance of the resonator occurs at 24 GHz, much lower than the design value 40 GHz. The SEM and optical microscope images of the fabricated resonator with a shunt inductor are shown in Fig. 4(c) and (d). Fig. 4(e) shows the measured response fitted with the circuit model to extract the inductance and Q of L_{shunt} , which are 0.61 nH and 8, respectively.

The inductance is close to the design value (0.66 nH); however, the resistive loss is 3.75 times larger than simulated. The high resistive loss is caused by two unexpected problems in the fabrication process: Firstly, the Al layer is partially etched in the step of removing the seed layer for electroplating. Secondly, the electroplated copper has a significant lower conductivity due to non-optimal plating recipe. These issues can be fixed upon further optimizations in future fabrications.

B. MEMS Filter with Shunt Inductors

The SEM image, the measured and simulated performance of the fabricated filter are shown in Fig. 5(a), (b) and (c). The simulation #1 represents the desired response with the key circuit parameters listed in Table 1. The simulation #2 uses the self-inductance, parasitic capacitance, and resistive loss extracted from the comprising structures, which are larger than the values predicted by EM simulations. The simulation #2 is consistent with the measurement results, while there is a 5-dB difference in the passband IL and a 6-dB difference in the stop band IL between the measurement and simulation #1. The discrepancy in the stopband is mainly caused by the parasitic capacitances between the lead lines. As seen in Fig. 5(a), the lead

lines are long and cause considerable parasitic coupling. As mentioned in Section A, the resistive loss is 3.75 times larger than simulation, which contributes to a 3.7 dB drop in the passband IL. The second cause of the increase in passband IL is the resonator Q of 146 being lower than the 500 in simulation (achieved in a previous fabrication run). This contributes to the other 1.3 dB difference in passband IL. The filter performance can be much improved in future designs by reducing L_s , C_f , and R_L , and enhance the fabrication yield in producing resonators of Q around 500 and higher.

IV. CONCLUSION

In this work, a wideband hybrid monolithic acoustic filter in the K-band is designed with co-simulation of the EM and acoustic domains. This work has demonstrated an FBW exceeding the k_t^2 limitation on FBW typically seen in acoustic filters while maintaining a small footprint of 1.4 mm². The filter performance presented in this paper is far from the limit and can be improved by resolving high resistive loss currently plaguing the electroplated copper.

REFERENCES

- F. A. Miranda and G. Subramanyam, "Design and development of ferroelectric tunable microwave components for ku- and k-band satellite communication systems," *IEEE Trans. Microw. Theory Tech.*, 2000.
- [2] T. Takai et al., "I.H.P. SAW technology and its application to microacoustic components (Invited)," in *IEEE International Ultrasonics* Symposium, IUS, 2017.
- [3] R. Ruby, R. Parker, and D. Feld, "Method of extracting unloaded q applied across different resonator technologies," in *Proceedings - IEEE Ultrasonics Symposium*, 2008.
- [4] M. Rinaldi, C. Zuniga, C. Zuo, and G. Piazza, "Super-High-Frequency Two-Port AlN Applications," *IEEE Trans. Ultrason. Ferroelectr. Freq. Control*, vol. 57, no. 1, pp. 38–45, 2010.
- [5] M. Hara, T. Yokoyama, T. Sakashita, M. Ueda, and Y. Satoh, "A study of the thin film bulk acoustic resonator filters in several ten GHz band," in *Proceedings - IEEE Ultrasonics Symposium*, 2009.
- [6] Y. Yang, R. Lu, T. Manzaneque, and S. Gong, "Toward Ka Band Acoustics: Lithium Niobate Asymmetrical Mode Piezoelectric MEMS Resonators," in 2018 IEEE International Frequency Control Symposium, IFCS, 2018, pp. 1-5.
- [7] G. Chen and M. Rinaldi, "High-Q X Band Aluminum Nitride Combined Overtone Resonators," in 2019 IEEE Int. Freq. Control Symp. Proc., 2019.
- [8] Y. Yang, R. Lu and S. Gong, "Scaling Acoustic Filters Towards 5G," 2018 IEEE International Electron Devices Meeting (IEDM), San Francisco, CA, 2018, pp. 39.6.1-39.6.4.
- [9] D. Psychogiou, R. Gómez-García, and D. Peroulis, "SAW-based bandpass filters with flat in-band group delay and enhanced fractional bandwidth," in 2017 IEEE MTT-S International Microwave Workshop Series on Advanced Materials and Processes for RF and THz Applications (IMWS-AMP), 2017, pp. 1–3.
- [10] C. Zuo, C. He, W. Cheng, and Z. Wang, "Hybrid Filter Design for 5G using IPD and Acoustic Technologies," in 2019 IEEE International Ultrasonics Symposium, 2019, pp. 1–4.
- [11] W. N. Allen, A. Gao, S. Gong, and D. Peroulis, "Hybrid Bandpass-Absorptive-Bandstop Magnetically Coupled Acoustic-Wave-Lumped-Element-Resonator Filters," *IEEE Microw. Wirel. Components Lett.*, 2018
- [12] Y. Yang, L. Gao, and S. Gong, "An X-band Lithium Niobate Acoustic RFFE Filter with FBW of 3.45% and IL of 2.7 dB," in 2020 MTT-S International Microwave Symposium (IMS), 2020, pp. 1-4.